Length scales of turbulence in stably stratified mixing layers

William D. Smyth[a] and James N. Moum
College of Oceanic and Atmospheric Sciences, Oregon State University, Corvallis, Oregon 97331-5503

(Received 19 January 1999; accepted 18 February 2000)

Turbulence resulting from Kelvin–Helmholtz instability in layers of localized stratification and shear is studied by means of direct numerical simulation. Our objective is to present a comprehensive description of the turbulence evolution in terms of simple, conceptual pictures of shear–buoyancy interaction that have been developed previously based on assumptions of spatially uniform stratification and shear. To this end, we examine the evolution of various length scales that are commonly used to characterize the physical state of a turbulent flow. Evolving layer thicknesses and overturning scales are described, as are the Ozmidov, Corrsin, and Kolmogorov scales. These considerations enable us to provide an enhanced understanding of the relationships between uniform-gradient and localized-gradient models for sheared, stratified turbulence. We show that the ratio of the Ozmidov scale to the Thorpe scale provides a useful indicator of the age of a turbulent event resulting from Kelvin–Helmholtz instability. © *2000 American Institute of Physics.* [S1070-6631(00)02206-6]

I. INTRODUCTION

The development of small-scale geophysical turbulence is governed largely by a competition between the vertical shear of the background flow and buoyancy forces due to ambient density stratification. Shear supplies kinetic energy for turbulent motions, while buoyancy effects (in stable stratification) act to reduce turbulence. The influences of these two factors have been investigated, both separately and together, in theoretical, experimental, observational, and numerical studies over the past several decades.[1–4]

Turbulence evolution in a stratified shear flow is determined not only by the strengths of the background shear and stratification, but also by the vertical distributions of those quantities. Two particular special cases have been employed extensively. The first is in most respects the simplest, while the second provides a more realistic model for geophysical flows. The simpler scenario is the one in which both background horizontal velocity and density vary linearly in the vertical coordinate, so that shear and stratification are uniform. Much of what we know about sheared, stratified turbulence is derived from the study of this idealized flow. A second important special case is the stratified shear layer, in which both shear and stratification are confined to a finite, horizontal layer. This localization of the shear leads to the possibility of inflectional instability, through which normal mode disturbances grow exponentially. In stably stratified conditions, this mechanism is called Kelvin–Helmholtz (KH) instability, and is thought to be an important source of turbulence in geophysical flows.[5–7]

The main goal of the present study is to clarify the relationship between the two special cases described above. Specifically, we will describe the evolution of turbulence resulting from KH instability in the context of a very useful conceptual picture derived mainly from the study of uniform shear and stratification. Since that conceptual picture is most readily understood in terms of the various length scales that characterize turbulence, our focus will be on issues of length scale evolution. We now describe this scenario, paraphrasing ideas developed mainly in the laboratory studies of Van Atta and co-workers,[8–13] in the analyses of Gibson,[14–17] and in the related work of Ivey and Imberger.[18,19] The central results may be derived through the use of simplified model equations for the turbulent kinetic energy.[10,20,21]

We begin by imagining a background flow characterized by uniform stratification and zero shear [Fig. 1(a)]. Suppose that, within this flow, a horizontal layer of thickness h is subjected to vigorous stirring, after which the resulting turbulence is allowed to decay. Buoyancy effects act preferentially on the larger scales of motion; an estimate of the smallest scale influenced by buoyancy is provided by the Ozmidov scale, $L_O = \sqrt{\epsilon/N^3}$ (in which ϵ is the turbulent kinetic energy dissipation rate and N the ambient buoyancy frequency). If the initial stirring is sufficiently energetic, L_O will initially be larger than the largest scale of turbulent motion (i.e., the layer depth), so that buoyancy will have negligible effect on the dynamics. As the flow evolves, however, both the largest and the smallest scales of the turbulence will increase in size, while the Ozmidov scale will decrease. Buoyancy will therefore become important eventually, deforming the largest scales of the turbulence first, the smaller scales later. Ultimately, all scales of the turbulence will be actively inhibited by buoyancy.

The evolution of an impulsively generated turbulent layer in a stratified environment can therefore be divided into three intervals: at first, the turbulence is unaffected by buoyancy; later, the large scales are affected but the smaller scales are not; finally, turbulence is suppressed by buoyancy on all scales. Gibson[14] referred to the first transition as the ''onset

[a]Author to whom all correspondence should be addressed; electronic mail: smyth@oce.orst.edu

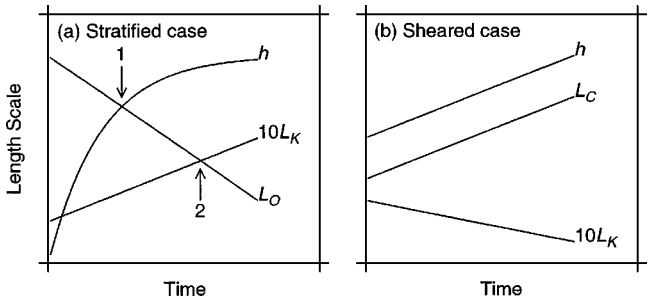

FIG. 1. Schematic representations of turbulent length scale evolution in environments with (a) uniform stratification and no shear, and (b) uniform shear and no stratification. Turbulence is generated impulsively at $t=0$ in a layer of thickness h. L_K, L_C, and L_O are the Kolmogorov, Corrsin, and Ozmidov scales, respectively. Arrows on (a) indicate (1) the onset of buoyancy control and (2) the BIV transition.

of buoyancy control'' (the point at which buoyancy begins to damp the largest scales), and to the second as the ''buoyant–inertial–viscous (BIV) transition'' (because buoyant, inertial, and viscous forces are of equal importance at that juncture). The BIV transition is thought to occur when eddies in the dissipative subrange are first affected by buoyancy, i.e., when L_O decreases below approximately ten times the Kolmogorov scale. Flow in the third stage of evolution was given the name ''fossil turbulence,'' a concept that has stimulated much discussion in the literature.[22–25]

We now consider the opposite case: a turbulent layer in a uniformly sheared, unstratified environment [Fig. 1(b)]. Like buoyancy, shear acts preferentially to deform the largest eddies; eddies much smaller than $L_C=\sqrt{\epsilon/S^3}$ (where S is the background shear) are unaffected. However, this deformation does not damp turbulent motions, but rather leads to Reynolds stresses through which turbulence grows at the expense of the background shear. In this case, both the energy of the turbulence and the range of length scales it occupies grow monotonically in time (the largest scale increases; the smallest decreases). The dissipation rate ϵ also increases in time, and therefore so does L_C. This limitless growth is possible because the uniform background shear provides an infinite source of kinetic energy.

The combined influence of uniform background shear and stratification has been investigated more recently.[10,12,13,26,27] If the background shear S is sufficiently weak in relation to N, the resulting evolution will be qualitatively the same as seen in the stratified case, and turbulence will ultimately be damped. On the other hand, if the shear is strong compared with the stratification, the evolution will be qualitatively similar to that found in unstratified shear flow. The effect of buoyancy remains confined to the largest scales of motion, and the turbulence is never damped. These two regimes are separated by a critical value of the bulk Richardson number $\mathrm{Ri}=N^2/S^2$ that appears to be close to 1/4.

Our subject in the present paper is the alternative case in which background shear and stratification are not spatially uniform, but rather are localized in a finite layer. Turbulence in both homogeneous and stratified mixing layers has been the object of many laboratory experiments,[28–33] theoretical studies,[34–41] and numerical simulations.[42–52] Observational studies have confirmed the utility of the stratified mixing layer model in interpreting geophysical mixing processes.[5–7,53] Turbulence generation via KH instability of a stratified mixing layer differs from the above-described uniform-gradient case in that shear and stratification are confined to a finite layer which expands in time, so that both S and N decrease. Moreover, S decreases more rapidly than N, with the result that any initial stratification, however weak, will eventually prevail over the shear and damp the turbulence. Thus, localized shear and stratification interact in ways that are fundamentally different from the interaction of uniform shear and stratification. If the initial bulk Richardson number Ri_0 exceeds its critical value (which is once again in the vicinity of 1/4), turbulence decays, as in the uniform case. In this paper, we will show that if Ri_0 is small, the evolution resembles the above-described pure shear case [Fig. 1(b)] at early times, the pure stratification case [Fig. 1(a)] at later times.

The onset of buoyancy control is not a useful concept for the KH case because, as we will see, the largest scales of the turbulence are affected by buoyancy right from the outset. This is not surprising, since the large eddies are Kelvin–Helmholtz billows, whose growth rate is controlled by the initial bulk Richardson number. Our purpose here will be to describe the encroachment of buoyancy effects on successively smaller length scales until turbulence is ultimately damped. The second transition described earlier, the BIV transition, is therefore relevant.

We begin in Sec. II with a description of the mathematical model and the numerical techniques employed to obtain solutions. In Sec. III, we discuss the evolutionary patterns of various length scales associated with the turbulent mixing layers. We begin by investigating the growth of the turbulent layer and compare the results with previous laboratory experiments. A result of central importance is that, as in laboratory flows, the bulk Richardson number evolves toward a quasiuniversal value somewhat in excess of 1/4. We then describe various measures of parcel displacements and the relationships among them. The length scales above which shear and stratification are active are also discussed, along with the Kolmogorov scale. Comparisons among these various length scales allow us to understand the evolution of a stratified shear layer in terms of the conceptual pictures based on the above-described uniform shear and stratification. In Sec. IV, we compare several nondimensional numbers that describe aspects of the evolutionary state of a turbulent flow. A summary and closing discussion is given in Sec. V.

II. METHODOLOGY

In this section, we describe the mathematical model that we use to represent turbulence in a sheared, stratified environment. We then discuss the numerical methods employed to solve the equations, and the initial conditions for the sequence of simulations whose results are described in the remainder of the paper.

A. The mathematical model

Our mathematical model employs the Boussinesq equations for velocity, density, and pressure in a nonrotating physical space measured by the Cartesian coordinates x, y, and z:

$$\frac{\partial \mathbf{u}}{\partial t} = \mathbf{u} \times (\nabla \times \mathbf{u}) - \nabla \Pi + g\,\theta \hat{k} + \nu \nabla^2 \mathbf{u}, \tag{1}$$

$$\Pi = \frac{p}{\rho_0} + K. \tag{2}$$

Here, p is the pressure, ρ_0 is a constant density scale, and $K = \frac{1}{2}\mathbf{u}\cdot\mathbf{u}$ is the specific kinetic energy. The thermodynamic variable θ represents the fractional specific volume deviation, or minus the fractional density deviation, i.e., $\theta = -(\rho - \rho_0)/\rho_0$, in which ρ_0 is a constant mean density. In a fluid where density is controlled only by temperature, θ is proportional to the temperature deviation (with proportionality constant equal to the thermal expansion coefficient). The vertical unit vector is represented by $\hat{k}$. The gravitational acceleration g has the value 9.8 m/s^2. Viscous effects are represented by the usual Laplacian operator, with kinematic viscosity $\nu = 1.0 \times 10^{-6}$ m^2/s. (Although many of our results will be presented in dimensionless form for application in a broad range of fluid dynamical problems, we also specify these dimensional quantities to facilitate comparison with observations of ocean turbulence.)

The augmented pressure field Π is specified implicitly by the incompressibility condition

$$\nabla \cdot \mathbf{u} = 0, \tag{3}$$

and the scalar θ evolves in accordance with

$$\frac{\partial \theta}{\partial t} = -\mathbf{u}\cdot\nabla\theta + \kappa \nabla^2 \theta, \tag{4}$$

in which κ represents the molecular diffusivity of θ.

We assume periodicity in the horizontal dimensions:

$$f(x + L_x, y, z) = f(x, y + L_y, z) = f(x, y, z), \tag{5}$$

in which f is any solution field and the periodicity intervals L_x and L_y are constants. At the upper and lower boundaries ($z = \pm \frac{1}{2}L_z$), we impose an impermeability condition on the vertical velocity:

$$w\big|_{z = \pm (1/2)L_z} = 0, \tag{6}$$

and zero-flux conditions on the horizontal velocity components u and v and on θ:

$$\left.\frac{\partial u}{\partial z}\right|_{z = \pm (1/2)L_z} = \left.\frac{\partial v}{\partial z}\right|_{z = \pm (1/2)L_z} = \left.\frac{\partial \theta}{\partial z}\right|_{z = \pm (1/2)L_z} = 0. \tag{7}$$

These imply a condition on Π at the upper and lower boundaries:

$$\left[\frac{\partial \Pi}{\partial z} - g\,\theta\right]_{z = \pm (1/2)L_z} = 0. \tag{8}$$

B. Initial conditions

The model is initialized with a parallel flow in which shear and stratification are concentrated in the shear layer, a horizontal layer surrounding the plane $z = 0$,

$$\tilde{u}(z) = \frac{u_0}{2} \tanh \frac{2z}{h_0}, \tag{9}$$

$$\tilde{\theta}(z) = \frac{\theta_0}{2} \tanh \frac{2z}{h_0}. \tag{10}$$

The constants h_0, u_0, and θ_0 represent the initial thickness of the shear layer and the changes in velocity and density across it. (Note that the shear layer and the stratified layer share a common initial thickness, h_0, in our model. Alternative choices are possible, for example, molecular processes favor a scenario in which shear layer depth exceeds stratified layer depth. Such flows may become unstable to Holmboe waves.[1,54,55] However, large-scale forcing mechanisms such as internal gravity waves exhibit no such preference. Since the latter class of processes is of primary interest to us, we find it simplest to assume that the layers have equal initial thickness.) The constants appearing in (9) and (10) can be combined with the fluid parameters ν and κ and the geophysical parameter g to form three dimensionless groups whose values determine the stability of the flow at $t = 0$:

$$\mathrm{Re}_0 \equiv \frac{u_0 h_0}{\nu}, \quad \mathrm{Ri}_0 \equiv \frac{g\,\theta_0 h_0}{u_0^2}, \quad \mathrm{Pr} \equiv \frac{\nu}{\kappa}. \tag{11}$$

The initial macroscale Reynolds number, Re_0, expresses the relative importance of viscous effects. In the present simulations, Re_0 is of order a few thousand, large enough that the initial instability is nearly inviscid. The bulk Richardson number, Ri_0, quantifies the relative importance of shear and stratification. If $\mathrm{Ri}_0 < 1/4$, the initial mean flow possesses unstable normal modes.[36] The Prandtl number, Pr, is the ratio of the diffusivities of momentum and density.

In order to obtain a fully turbulent flow efficiently, we add to the initial mean profiles a perturbation field designed to approximate the structure of the most-unstable primary and secondary instabilities. The horizontal velocity perturbation is given by

$$\hat{u}(x,z) = \frac{u_0}{2}\frac{1}{k_0}\left(-\cos\frac{2k_0 x}{h_0} + 2b\cos\frac{k_0 x}{h_0}\right)\tanh\frac{2z}{h_0}\,\mathrm{sech}\,\frac{2z}{h_0}, \tag{12}$$

where k_0 is the streamwise wave number of the fastest-growing eigenmode of the parallel flow. (While this perturbation projects onto both the primary and pairing instabilities, the phase relationship between the two modes is *not* chosen to optimize pairing. The flow must adjust itself to achieve the correct phase relationship before pairing can occur.[41,56,57])

In order to excite three-dimensional secondary instabilities, the spanwise velocity is given a quasirandom perturbation,

$$\hat{v}(x,y,z) = \frac{u_0}{2} r_v(x,y,z)\,\mathrm{sech}^2\frac{2z}{h_0}, \tag{13}$$

where $r_v(x,y,z)$ is a random function varying between -1 and 1, designed so that $\hat{v}$ will have zero mean and zero vertical integral. Because of the latter condition, it is possible to obtain $\hat{w}(x,y,z)$, the perturbation vertical velocity field corresponding to (12) and (13), simply by integrating (3) in the vertical. Finally, a random perturbation is applied to the scalar field, viz.

$$\hat{\theta}(x,y,z)=\frac{\theta_0}{2}r_\theta(x,y,z)\,\mathrm{sech}^2\frac{2z}{h_0}, \tag{14}$$

where r_θ is a random function with zero mean, varying between -1 and 1.

The initial condition is now defined by

$$\begin{aligned}&\theta=\tilde{\theta}(z)+a\,\hat{\theta}(x,y,z), \quad u=\tilde{u}(z)+a\hat{u}(x,y,z),\\ &v=a\hat{v}(x,y,z), \quad w=a\hat{w}(x,y,z),\end{aligned} \tag{15}$$

where a is a constant controlling the amplitude of the initial perturbation.

C. Numerical methods

Because the horizontal boundary conditions are periodic, discretization of the horizontal differential operators is accomplished efficiently in Fourier space using fast Fourier transforms. In the vertical direction, spatial discretization is done using second-order, centered finite differences, in order to retain flexibility in the choice of upper and lower boundary conditions. The largest-scale runs described here employ array sizes of $512\times64\times256$, which requires about 800 Mbytes of main memory on a 32-node CM5 partition. Although the geometry of the computational grid inevitably excludes some modes that would be present at both large and small scales, it is designed to accommodate those modes which contribute most to the dynamics of the turbulence, allowing us to simulate flows with the highest possible Reynolds number for a given memory capacity.

It is now generally recognized that a reliable direct numerical simulation (DNS) code must have grid spacing no greater than a few (3–6) times the Kolmogorov length scale $L_K=(\nu^3/\epsilon)^{1/4}$ in which ϵ is the volume-averaged kinetic energy dissipation rate.[58] For flows with $\mathrm{Pr}>1$, the Kolmogorov scale is replaced by the Batchelor scale: $L_B=L_K/\mathrm{Pr}^{1/2}$. In order to take advantage of this information, one must be able to estimate the maximum value of ϵ in advance. We do this by employing the scaling $\epsilon^+=cu_0^3/h_0$. Through trial and error, we have established the value 6.5×10^{-4} for the proportionality constant c. The grid spacing is then set to $2.5L_B^-$, where L_B^- is the estimated minimum Batchelor scale $(\nu^3/\epsilon^+)^{1/4}\,\mathrm{Pr}^{-1/2}$. The present version of the model uses isotropic grid resolution, i.e., $\Delta x=\Delta y=\Delta z$. These choices are validated in Sec. II E, using a stringent spectral test of grid resolution.

The fields are stepped forward in time using a second-order Adams–Bashforth method. Implicit time stepping of the viscous operators has turned out to be unnecessary, as the time step is limited by the advective terms. For accuracy and numerical stability, we limit the time step in accordance with

$$\Delta t<0.12\min_{i=1,3}\left(\frac{\Delta x_i}{U_i^+}\right), \tag{16}$$

in which U_i^+ is the maximum speed in the x_i coordinate direction. At each time step, the augmented pressure field is obtained as the solution of a Helmholtz equation which is designed to force the flow to be nondivergent at the next time step. To control aliasing effects, the upper 16% of wave numbers in each spatial dimension are filtered out of the velocity fields every 1–50 time steps, depending on the amount of energy present in those modes. This filtering also serves to remove contamination by small-scale pressure modes which arise due to our choice of vertical discretization. The energy removed by filtering is monitored to ensure that it remains small (rarely more than a few percent, never more than 20%) compared with the energy removed by the molecular viscosity term. (This adaptive de-aliasing scheme is useful because of the nonstationary nature of the turbulence. The most intense turbulence, and therefore the smallest Kolmogorov scale, occurs during a relatively brief phase of each simulation. Because the grid resolution is chosen to be adequate for that phase, it is much more than adequate during the remainder of each run, i.e., the energy levels in the smallest resolved scales are often negligible. Because de-aliasing requires significant processing time, we economize by de-aliasing only to the degree that the procedure is required.) In the present application, selected scalar quantities are saved at every time step, while the full three-dimensional fields are saved at intervals of $10h_0/u_0$.

D. Parameter values

The model equations can be nondimensionalized using u_0, h_0, and θ_0 as scales for velocity, length, and fractional density fluctuation. The resulting nondimensional equation are completely specified by the parameter set (Pr, Ri_0, Re_0), and the dataset used here is designed to explicate effects of variations in the values of these three parameters. Before discussing them further, however, we will first describe our choices for several secondary parameters that appear in the boundary and initial conditions.

The boundary conditions, once nondimensionalized, introduce three additional parameters: L_x/h_0, L_y/h_0, and L_z/h_0. By taking advantage of the known geometry of the outer scales of turbulent KH billows, we are able to choose these parameters for maximally efficient use of memory while minimizing boundary effects. These choices are based on results from linear stability analyses of the parallel flow,[37,59] two-dimensional nonlinear simulations with various domain sizes,[56] and secondary stability analyses of large-amplitude, two-dimensional KH waves.[38,39,41,55] For all runs, we choose $L_x/h_0=4\pi/k_0h_0=14.0$, in order to allow for a single pairing of the primary KH wave train. This imposes no significant restriction on the flow evolution as long as Ri_0 is not too small; accordingly, we keep $\mathrm{Ri}_0\geqslant0.08$. The vertical domain size L_z/h_0 is set to 6.95 for all cases. This choice is based on extensive sensitivity tests, some of which are reported in a separate publication.[56] The spanwise domain size is given one of two values: $L_y/h_0=3.50$ or 1.75, which

TABLE I. Parameter values describing a sequence of eight simulations of breaking Kelvin–Helmholtz billows. N_x, N_y, and N_z are the array dimensions, L_x, L_y, and L_z are the domain dimensions, and Δx ($=\Delta y=\Delta z$) is the grid interval. Initial conditions are characterized by the length scale h_0, the velocity scale u_0, and the temperature scale θ_0. $L_{sc}=u_0^2/4g\theta_0$ is an estimated lower bound on the final layer depth based on the assumption that the bulk Richardson number asymptotes to 1/4. Pr is the Prandtl number; Ri_0 and Re_0 are the initial bulk Richardson and Reynolds numbers, respectively. $\mathrm{Re}_f=\mathrm{Re}_0/2\mathrm{Ri}_0$ is a lower bound on the final value of the Reynolds number based on the assumption that the bulk Richardson number asymptotes to 1/4. Simulations are labeled as RxxPy, where ''xx'' represents $\mathrm{Re}_f/1000$ and ''y'' represents Pr.

Run	R06P1	R16P1	R04P1	R10P1	R03P1	R04P4	R06P4	R04P7
N_x	256	512	256	512	256	512	512	512
N_y	64	64	64	64	64	64	64	64
N_z	128	256	128	256	128	256	256	256
L_x (m)	3.29	5.24	3.29	5.24	3.29	3.29	3.29	2.73
L_y (m)	0.82	0.65	0.82	0.66	0.82	0.41	0.41	0.34
L_z (m)	1.63	2.62	1.63	2.60	1.63	1.63	1.63	1.36
$\Delta x(10^{-2}$ m)	1.29	1.03	1.29	1.02	1.29	0.64	0.64	0.53
h_0 (m)	0.24	0.38	0.24	0.38	0.24	0.24	0.24	0.20
$u_0(10^{-3}$ m/s)	8.34	13.27	8.34	13.27	8.34	8.36	8.34	8.34
$\theta_0(10^{-6}$ K)	2.41	3.83	3.61	5.75	4.81	3.70	2.41	2.00
L_{sc} (m)	0.74	1.17	0.49	0.78	0.37	0.48	0.74	0.89
Pr	1	1	1	1	1	4	4	7
Ri_0	0.08	0.08	0.12	0.12	0.16	0.12	0.08	0.08
Re_0	1965	4978	1967	4978	1967	1967	1967	1354
Re_f	6140	15 557	4098	10 371	3074	4119	6147	4232
Symbol	○	⊗	▽	△	◇	◁	○	●

allow for either four or two (approximate) wavelengths of the dominant secondary instability.[41] We believe that two wavelengths is sufficient; four wavelengths were employed in selected runs as a check on this assumption.

The flow evolution is also affected by the initial conditions. Once nondimensionalized by u_0, h_0, and θ_0, these are specified by the wave number k_0, the amplitude parameters a and b, and by the form of the random noise fields r_v and r_θ. We ignore the slight dependence of k_0 on the Richardson number[37] and use $k_0=0.90/h_0$ for all simulations. The amplitude parameter a appearing in (15) is given the value 0.05, which ensures that the simulation approximates the growth of infinitesimal perturbations. The parameter b, from (12), is given the value 0.4177. This choice dictates that the subharmonic mode will be initialized with one-half the kinetic energy of the primary. Auxiliary runs were conducted to assess the influence of the random noise fields. Although the detailed evolution of the flow is highly sensitive to the initial conditions, the statistical quantities that are of primary concern to us are not.

E. Overview of turbulence evolution

In this paper, we describe results from a sequence of eight simulations designed to explicate the effects of Ri_0, Re_0, and Pr, with the above-mentioned choices for the remaining parameters. Parameter values for these simulations are summarized in Table I. In each simulation, the flow evolution is qualitatively similar to that shown in Fig. 2. The initial growth and pairing of the primary KH vortices [Fig. 2(a)] is followed by a breaking phase, in which turbulence is created via three-dimensional secondary instabilities [Figs. 2(b) and 2(c)]. A detailed description of this process has been given recently by Cortesi *et al.*[51]) Finally, there ensues an extended period in which turbulence gradually becomes anisotropic and ultimately decays. The flow thus relaxes toward a dynamically stable, parallel configuration perturbed by laminar gravity waves [Fig. 2(d)].

Next, we examine spectra of kinetic energy [Fig. 3(a)] and scalar variance [Fig. 3(b)] taken from the most-turbulent phase of simulation R04P7. At this point in this high-Prandtl number (Pr=7) simulation, the DNS solution is expected to represent a useful model of turbulence in thermally stratified water. This flow state also represents a severe test of model resolution. Spectra are computed over the central region $\{0<y\leqslant L_y, \frac{7}{16}L_z<z\leqslant\frac{9}{16}L_z\}$, then averaged. Turbulence is very nearly homogeneous in this region; nevertheless, Kolmogorov and Batchelor scalings are applied separately to spectra computed at each (y,z) prior to averaging. Spectra are terminated at a wave number equal to 0.84 times the Nyquist limit, beyond which the de-aliasing filter is active. In addition to the computed kinetic energy spectrum, Fig. 3(a) includes two standard spectral forms against which measured energy spectra are often compared.[5] The solid curve represents the Nasmyth spectrum,[60] which was derived from measurements made in a tidal channel. The dashed curve is the theoretical spectrum derived by Panchev and Kesich.[61] In the dissipation range ($0.1<k_xL_K<1$), the three curves agree closely. At the smallest resolved scales, spectrum rolls off at a rate intermediate between the Nasmyth and Panchev–Kesich forms. Note that this flow realization exhibits a complete dissipation subrange, but only the beginning of an inertial range. This compromise is necessary in order to achieve the high Prandtl number characteristic of thermally stratified water. Simulations with Pr=1 exhibit up to a decade of inertial range.[62,63]

The scalar variance spectrum [Fig. 3(b)] is also compared with two standard forms. The dashed curve represents the Batchelor spectrum.[64] The solid curve shows a more

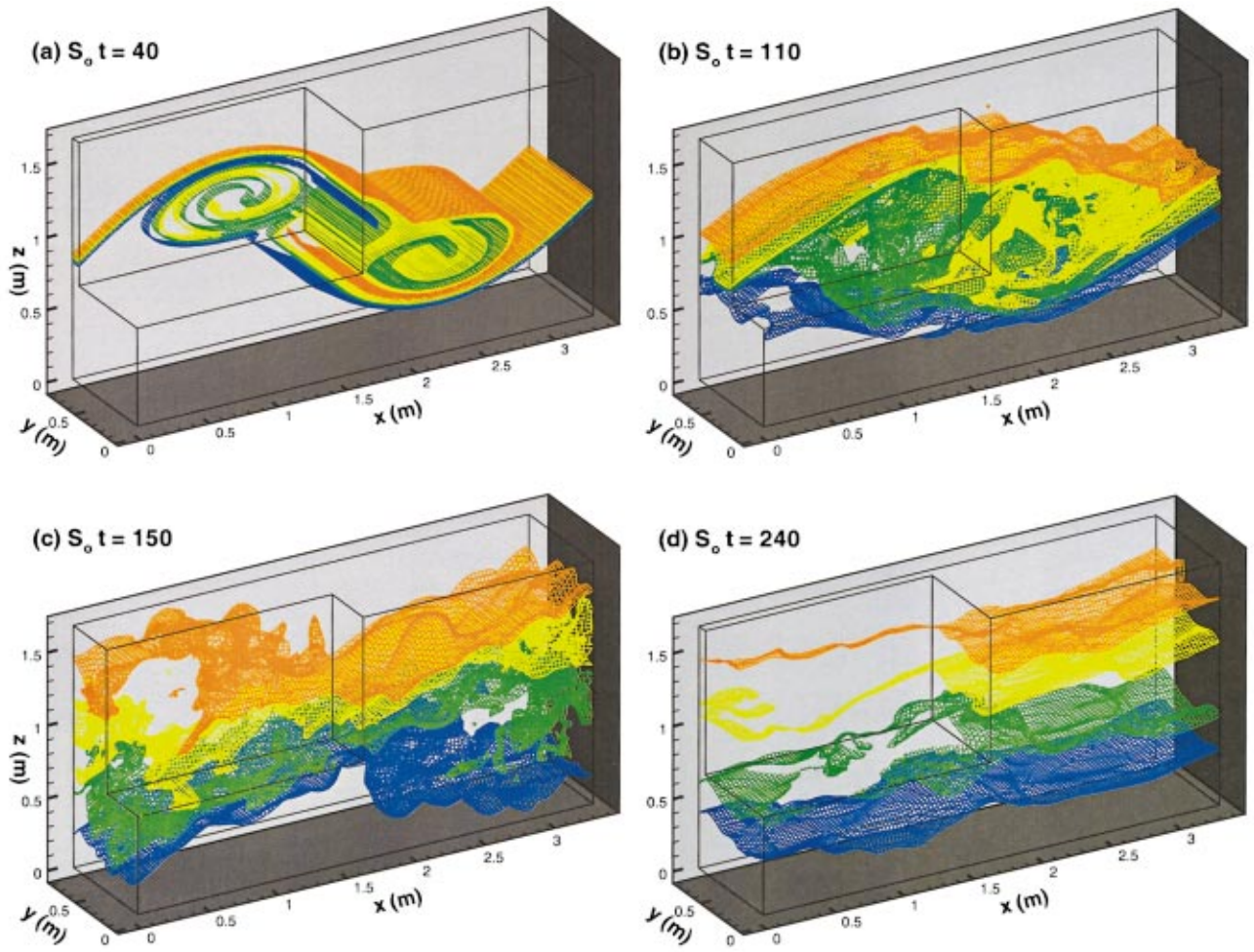

FIG. 2. (Color) Life cycle of a breaking KH wave train from simulation R06P1, visualized by isotherms. The blue, green, yellow, and orange surfaces represent $2\theta/\theta_0=(-0.67,-0.17,0.17,0.67)$, respectively. Times are expressed in units of $S_0^{-1}=28.28$ s. S_0 is the maximum shear of the initial velocity profile.

complete theoretical form derived by Kraichnan[65,66] on the basis of the Lagrangian history direct interaction approximation (LHDIA). The DNS spectrum strongly favors the LHDIA form. (A detailed discussion of the physics of the scalar spectrum is given in a separate publication.[62]) The design criteria described in Sec. II C turned out to be conservative in this case: grid resolution extends well beyond the Batchelor scale. In each spectrum, the absence of increased energy at small scales indicates that the grid resolution has been chosen appropriately. We conclude that the model resolution is more than adequate for the present purposes.

We close this overview with a qualitative comparison of our simulated turbulent layers with the events they were originally designed to model: turbulent patches in the ocean thermocline. These comparisons will allow us to define and demonstrate the diagnostic techniques to be used later in the paper, and also to further illustrate the compromises that must be made in conducting direct simulations of turbulence in thermally stratified water. In Fig. 4(a), the solid curve in the left panel shows a segment of a high-resolution vertical temperature profile obtained 1000 km off the northern California coast in the spring of 1991.[67] To understand the nature of the observed turbulence, we need a description of the ''background'' environment in which the turbulence is evolving, not an easy thing to define when the data consist of a single profile. Following Thorpe,[68] we sort the raw temperature values into monotonically increasing order, as shown by the dashed curve. The result is an approximation to the profile that would be measured if the turbulence were allowed to relax adiabatically to a motionless state. The middle frame shows the Thorpe displacement $d_T(z)$, the excursion of the fluid parcel at z from the depth it occupies in the monotonically increasing configuration. The shape of this profile suggests the presence of an overturn spanning the entire turbulent layer. The rightmost panel shows the perturbation temperature, defined as the deviation from the monotonic profile.

Figures 4(b) and 4(c) show sample temperature and displacement profiles extracted from our DNS solutions. Each was selected at a stage in the simulation when the large-scale geometry resembled that shown in Fig. 4(a), i.e., a turbulent layer dominated by a single large overturn. The main parameters that vary between Figs. 4(b) and 4(c) are the Reynolds and Prandtl numbers. In Fig. 4(b), the overall shape of the DNS profile resembles the observed profile, and both the spatial scale and the magnitude of the temperature fluctua-

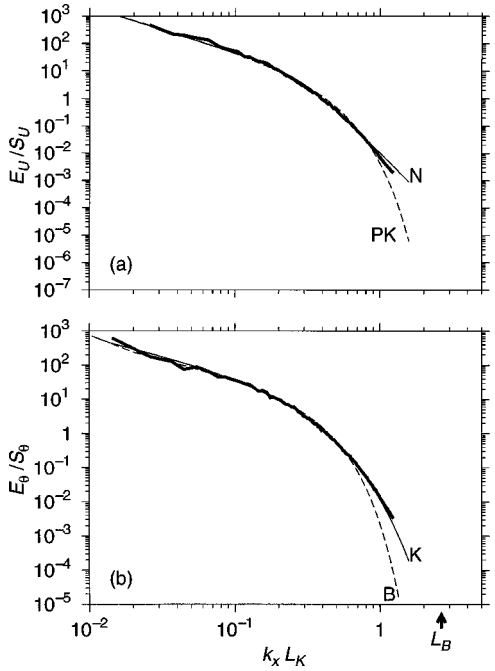

FIG. 3. Streamwise spectra of kinetic energy (a) and scalar variance (b) from simulation R04P7 at $S_0 t = 150$. For (a), the Kolmogorov scaling $S_U = (\bar{\epsilon}\nu^5)^{1/4}$ is employed. Thin curves represent the Nasmyth spectrum—Ref. 60 (solid) and the Panchev–Kesich spectrum—Ref. 61 (dashed). For (b), the Batchelor scaling $S_\theta = \bar{\chi} L_K^3/\kappa \, \mathrm{Pr}^{3/2}$ is employed. Thin curves represent the Kraichnan spectrum—Ref. 66 (solid) and the Batchelor spectrum—Ref. 76 (dashed). [Each theoretical spectral form involves an adjustable constant. Values for these constants are chosen by a fitting method described in detail by Smyth (Ref. 62). The values employed here in the Batchelor and Kraichnan spectra are $q_B = 6.18$ and $q_K = 8.38$, respectively.]

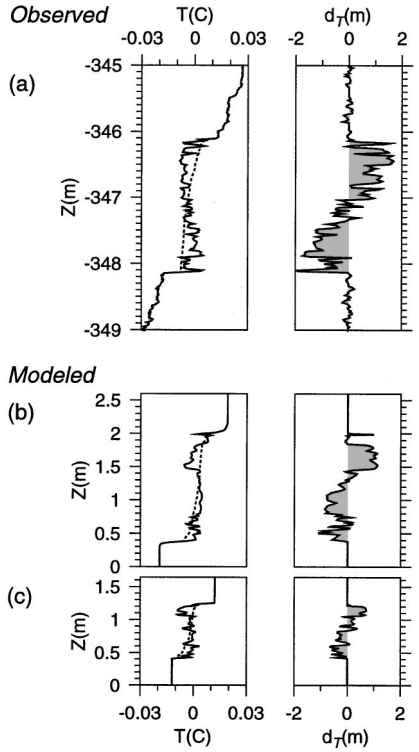

FIG. 4. Leftmost panels: Temperature fluctuation profiles based on observational data (Refs. 67 and 69) (a) and on the present DNS: R16P1 (b); R06P4 (c). Conversion of θ to T assumes a thermal expansion coefficient of $10^{-4}\,\mathrm{K}^{-1}$. Dashed lines represent the reordered profiles. Panels on the right show Thorpe displacement, the distance between a fluid parcel and its location in the reordered profile.

tions compare favorably. However, the observed profile exhibits considerably more small-scale structure than does the modeled profile. This is a Prandtl number effect: The Prandtl number of seawater is near 7, while the value used in the simulation shown in Fig. 4(b) is 1. In Fig. 4(c), we show similar diagnostics taken from a simulation with increased Prandtl number (Pr=4, in this case). Here, the degree of small-scale structure is more consistent with the observation, the cost being a reduction in thickness (and thus Reynolds number) of the turbulent layer. For this study, we have conducted eight simulations using a range of Reynolds and Prandtl numbers (Table I). With Pr=7, we are able to achieve Reynolds numbers characteristic of the smallest turbulent patches that have been observed in the ocean thermocline.[69] By reducing Pr to unity, we achieve much higher Reynolds numbers, but sacrifice temperature variance in the smallest scales.

We note in passing that Fig. 4 illustrates the main limitations of both observational and numerical approaches to the study of geophysical turbulence. Observational data give only a glimpse of any given turbulent event, and must therefore be supplemented by means of strong assumptions. In contrast, numerical models furnish comprehensive data, but have difficulty reaching the parameter range characteristic of the geophysical flows they are intended to represent.

In summary, our simulated stratified shear layers undergo a realistic transition process leading to a state that exhibits many characteristics in common with both theoretical models of fully developed turbulence and observations of turbulence in geophysical flows. As turbulence decays, the simulated layers evolve toward a stable, parallel configuration. In what follows, we examine the evolution of various turbulence length scales that allow us to characterize the flow physics at each stage of its evolution.

III. EVOLUTION OF TURBULENT LENGTH SCALES

Our goal in this section is to describe length scale evolution in a localized gradient model in terms of the conceptual pictures that have proven useful in the understanding of uniform gradient models. In Sec. III A, we describe the spreading of the sheared and stratified layers. We find that the bulk Richardson number evolves in a common manner over a wide range of parameter values, echoing results from the classic laboratory experiments of Thorpe[31] and Koop and Browand.[32] This finding is useful in three ways. First, it provides an additional measure of confidence in the realism of our model solutions. Second, it suggests a scaling for the turbulence length scales to be discussed later. Finally, the evolution of the bulk Richardson number will prove to be the crucial element that distinguishes turbulence in localized gradients from that found in uniform gradient models.

In Sec. III B we examine three length scales designed to quantify parcel displacements associated with the energy-bearing eddies. These include variations of the parcel-

reordering approach introduced by Thorpe.[68] In Sec. III C, we discuss the Ozmidov and Corrsin scales, which represent the smallest length scales at which the distorting influences of background stratification and shear (respectively) are felt. Using these results in combination with the eddy sizes computed in Sec. III B, we assess the degree to which the energy-containing eddies are influenced by background gradients at different stages in flow evolution. We then make a similar assessment with respect to the smaller-scale eddies in which viscous dissipation takes place.

The ultimate result of Sec. III is a summary of the evolution of turbulence resulting from the instability of a localized layer of nonzero shear and stratification (Sec. III D). The scenario is usefully understood as a combination of the limiting cases that occur in the uniform gradient model (cf. Fig. 1). The crux of the difference between the localized and uniform gradient models lies in the evolution of the bulk Richardson number.

A. Expansion of the sheared and stratified layers

In the present study, the initial thicknesses of the shear layer and the stratified layer were chosen to be equal. As the flow evolves, both of these thicknesses increase, and they do so at different rates. In addition, the shapes of the profiles evolve away from their initial hyperbolic tangent forms (9) and (10). The definition of the time-dependent depths of the shear and stratified layers is therefore somewhat arbitrary.

We look first at the evolutions of the integral scales, which are defined as follows using the profiles of horizontally averaged density $\overline{\theta}$ and velocity $\overline{u}$:

$$I_u = \int_{-L_z/2}^{L_z/2} \left[1 - \left(2\frac{\overline{u}}{u_0} \right)^2 \right] dz,$$
$$I_\theta = \int_{-L_z/2}^{L_z/2} \left[1 - \left(2\frac{\overline{\theta}}{\theta_0} \right)^2 \right] dz. \tag{17}$$

These length scales are defined so that their initial values equal h_0 [up to the factor $\tanh(L_z/h_0) \cong 1$]. In all eight simulations, I_θ and I_u grow from these original values to final values ranging from 0.45 to 1.55 m (Fig. 5). The final values vary by approximately a factor of 3 depending on the values of h_0, u_0, and θ_0.

In contrast, the bulk Richardson number formed from the integral scales,

$$\mathrm{Ri}_I = \frac{g\theta_0 / I_\theta}{(u_0 / I_u)^2}, \tag{18}$$

exhibits relatively uniform behavior, increasing from Ri_0 to a final value between 0.25 and 0.40 (Fig. 6). This result is consistent with observations of KH billows in the laboratory experiments of Thorpe[31] and Koop and Browand[32] In both of these studies, despite very different initial conditions and experimental techniques, final values of the bulk Richardson number were restricted to the range 0.32 ± 0.06.

The uniformity of the bulk Richardson number evolution suggests that much of the dependence of the integral scales upon the initial conditions may be collapsed through the use of a suitably defined length scale. Here, we define

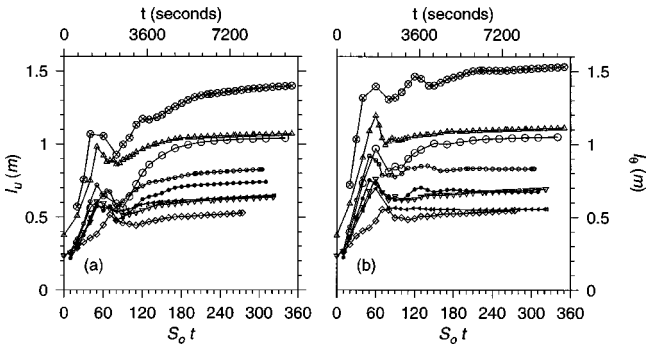

FIG. 5. Integral scale depths of the shear layer (a) and the stratified layer (b), shown at selected times during all eight simulations. Symbols indicate ''snapshots'' taken from different simulations as given in Table I. Time is given both in seconds and in units of the initial shear time scale $S_0^{-1} = h_0/u_0$, which is equal to 28.28 s for all simulations.

$$L_{\mathrm{sc}} = \frac{u_0^2}{4g\theta_0}. \tag{19}$$

The factor of 4 is inserted so that, if $I_\theta = I_u = L_{\mathrm{sc}}$, then $\mathrm{Ri}_I = 1/4$. L_{sc} may therefore be thought of as an approximate lower bound on the thickness the turbulent layer will attain once entrainment via billow growth and pairing is complete.

As shown in Fig. 7, this scaling removes much of the dependence on initial conditions seen in Fig. 5, and a characteristic pattern of evolution is clearly visible. In all cases, the layer depths increase dramatically during the initial growth and merging of the KH billows. This initial phase is followed by a rapid collapse as the billows break. During this phase, potential energy stored in the billows is converted to kinetic energy via secondary instability.[41,55] We then observe a second period of layer growth during which turbulence decays, followed by a prolonged period of slow spreading due to the action of molecular diffusion on the mean profiles. The shear layer and the stratified layer expand by similar amounts, though at different times: The initial billow growth expands the stratified layer preferentially, whereas in the turbulent phase following the collapse of the billows, the shear layer expands more rapidly. This pattern corresponds closely to that seen in laboratory experiments.[32] Not surprisingly,

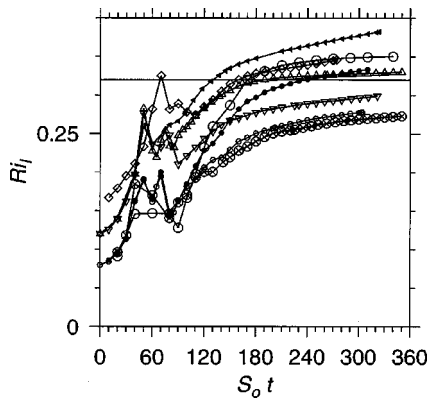

FIG. 6. Evolution of the bulk Richardson number. The horizontal line indicates Ri=0.32, the standard final value from laboratory experiments. Symbols are as defined in Table I.

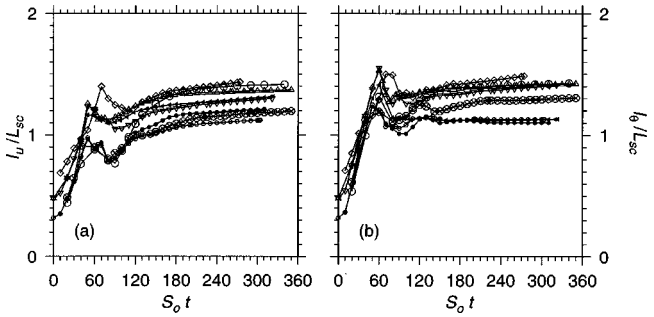

FIG. 7. Integral scale depths of the shear layer (a) and the stratified layer (b), scaled by $L_{sc}=u_0^2/4g\theta_0$. Symbols are as defined in Table I.

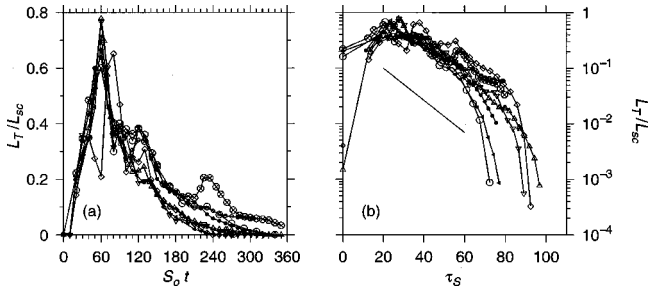

FIG. 8. Evolution of the standard Thorpe scale, L_T, averaged over the stratified layer V_s. Symbols are as defined in Table I. In (a), time is scaled as before using the initial maximum shear S_0. In (b), dimensional time is replaced by the nonlinear time scale $\tau_S=\int_0^t S(t')dt'$. The straight line indicates exponential decay with nondimensional *e*-folding time 15.

differences in the spreading of the stratified layer that are not collapsed by the above-described scaling are largely a function of the Prandtl number, with I_θ/L_{sc} increasing more in the Pr=1 cases than in the cases with Pr>1.

B. Parcel displacement scales

Our simulated flow fields invariably exhibit a sharp boundary between an inner, active region to which turbulence is confined, and an outer laminar region in which velocity and density are constant. In the analyses reported here, we prefer to compute certain statistics over the turbulent region only. The bulk thicknesses described in Sec. III A define layers which contain a considerable amount of nonturbulent fluid, and are therefore unsuitable for this purpose. Unfortunately, the turbulent region is difficult to define precisely. This problem is familiar in observational studies, where the definition of boundaries between which turbulence statistics should be calculated is always a challenge.[69] Here, we have found it most useful to compute statistics over the region in which significant density changes occur. Specifically, we define the upper and lower boundaries of the region of interest to be the isotherms $z_U(x,y,t)$ and $z_L(x,y,t)$ such that $\theta|_{z=z_U}=\alpha\theta_0/2$ and $\theta|_{z=z_L}=-\alpha\theta_0/2$, where $\alpha=\tanh(1)$. The inner region thus defined contains some wave motions as well as turbulence, and it may contain fluid which is stratified but not turbulent, but it has the virtue of containing all turbulent motions while being straightforward to identify. This inner region is denoted V_s.

We will also need to specify values for the buoyancy frequency $N(t)$ and the shear $S(t)$ that characterize the turbulent layer as a whole. One choice would be values based on the above-described integral scales, namely $S(t)=u_0/I_u(t)$ and $N(t)=\sqrt{g\theta_0/I_\theta(t)}$. However, these estimates are biased toward the maximum gradients found in the mean profiles. [For example, if $\overline{u}(z)$ is a hyperbolic tangent function, u_0/I_u is the maximum shear. If $\overline{u}(z)$ represents uniform shear over a finite layer of depth I_u, u_0/I_u overestimates that shear by 30%.] What we seek here are estimates based on the average gradients in the turbulent region V_s. Accordingly, we define the bulk gradients to be the average gradients of the mean profiles in layers defined analogously with V_s, viz.

$$S(t)=\frac{\alpha u_0}{h_u(t)}, \quad \theta_{0z}(t)=\frac{\alpha\theta_0}{h_\theta(t)}, \tag{20}$$

where h_u is the distance between the isotachs $\overline{u}=\pm\alpha u_0/2$ of the mean velocity and h_θ is the distance between the isotherms $\overline{\theta}=\pm\alpha\theta_0/2$ of the mean scaled temperature. The buoyancy frequency is then given by

$$N(t)=\sqrt{g\theta_{0z}(t)}. \tag{21}$$

The Thorpe scale,[68,70] L_T, is computed by adiabatically reordering our discrete vertical profiles of density so as to render them statically stable (cf. Fig. 4 and the accompanying discussion). We do this at each (x,y) in the computation domain and record the displacements needed to effect the reordering. L_T is then identified as the rms displacement within V_s. Like the layer depths, the Thorpe scale increases rapidly during the initial growth phase [Fig. 8(a)]. Unlike the layer depths, however, L_T then decreases and approaches zero as the turbulence decays. In Fig. 8(b), we show L_T as a function of a nonlinear time scale based on the evolving large eddy turnover time, S^{-1}: $\tau_S=\int_0^t S(t')dt'$. L_T reaches its maximum near $\tau_S=25$. Subsequent evolution tends to approximate exponential decay with nondimensional *e*-folding time near 15. This *e*-folding time may be approximated in dimensional terms as $15S^{-1}$, or as 1.3 times the buoyancy period, $2\pi N^{-1}$ (assuming $N^2/S^2\approx 1/4$). Exponential decay continues until $\tau_S\sim 60-80$, after which the decay becomes more rapid. Beyond this point, L_T is generally not much larger than the vertical grid spacing Δz, and the computation is suspect as a result.

A related measure of the length scale of density disturbances is the three-dimensional version of the Thorpe scale, L_{T3}, which is computed as above except that the scalar field $\theta(x,y,z)$ is reordered all at once rather than in columns. The fluid parcel located at (x,y,z) moves to the height z^* when the fluid is thus reordered,[71] and L_{T3} is the rms average of z^*-z over V_s. L_T is a measure of overturning only, whereas L_{T3} is a measure of scalar displacements in general. For example, in a nonoverturning wave field, $L_T=0$ whereas $L_{T3}\neq 0$. L_{T3} follows a pattern of growth and subsequent decay very similar to that exhibited by L_T [Fig. 9(a)]. Closer comparison shows that L_T and L_{T3} are close in value when large, but that L_{T3} exceeds L_T quite significantly when L_T is

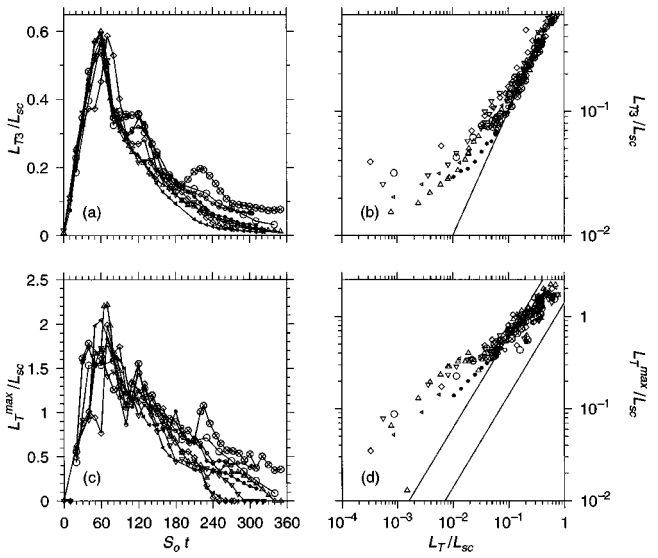

FIG. 9. Upper frames show the displacement scale based on three-dimensional reordering of the temperature field, vs time (a) and vs L_T (b). Lower frames show the maximum Thorpe scale vs time (c) and vs L_T (d). The upper and lower solid lines on (d) indicate $L_{Tmax}/L_T=6$ and $L_{Tmax}/L_T=\sqrt{2}$, respectively. Symbols are as defined in Table I.

small [Fig. 9(b)]. The small values of L_T occur at the beginning and end of each simulation, during which times there is little or no overturning, but there are significant wave-like disturbances whose presence is manifest in the value of L_{T3}.

A third measure of scalar displacements is the maximum value of the Thorpe displacement within V_s, denoted L_T^{max}. When the displacement field is dominated by a single large overturn, the ratio $L_T^{max}/L_T \approx \sqrt{2}$. When the displacement field is random (white), this ratio is six. As shown in Fig. 9(c), L_T^{max} attains values approximately twice the scale thickness of the turbulent layer before decreasing gradually to zero. The ratio L_T^{max}/L_T is generally between $\sqrt{2}$ and 6 when large overturns are present [Fig. 9(d)]. As the turbulence decays, the ratio becomes larger than 6, indicating the presence of isolated overturns in a field of otherwise stable stratification.

We continue with a look at three quantities which have been used extensively to estimate the energy-containing scales of stratified turbulence. The Ellison scale is given by

$$L_E=\frac{\theta'_{rms}}{\theta_{0z}}. \tag{22}$$

The numerator is the root-mean-square fluctuation of the scaled temperature θ about its horizontally averaged profile, $\overline{\theta}(z)$; the denominator is the bulk vertical temperature gradient defined in (20). A clear correlation between L_E and L_T is demonstrated in Fig. 10(a). There, the straight line indicates the result $L_E=L_T$, which was obtained by Itsweire[72] in laboratory experiments on grid-generated turbulence. A similar result has been obtained more recently from numerical simulations of a uniform-gradient model.[27] On average, our results are consistent with the above-cited results, but the rate of increase of $\log L_E$ with $\log L_T$ is distinctly different from unity. We attribute this to the fact that our background temperature gradient is not uniform. The bulk temperature gradient used in (22) is an overestimate of the true temperature gradient near the center of the turbulent layer where the fluid is well stirred (and local temperature fluctuations are large), and is an underestimate near the edges of the layer.

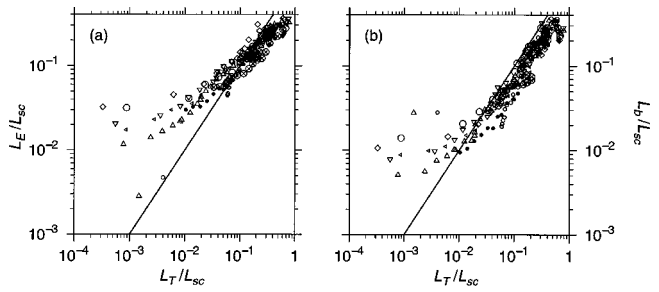

FIG. 10. Comparison between estimates of the size of the energy-containing eddies. (a) Ellison scale vs Thorpe scale. The line indicates the result $L_E \approx L_T$ derived from the laboratory experiments of Itsweire (Ref. 72). (b) The buoyancy scale. The straight line indicates median ratio $L_b/L_T=1.0$ derived from observations of turbulent patches in the ocean thermocline (Ref. 69).

We conclude this section with a look at the buoyancy scale, defined by

$$L_b=\frac{w'_{rms}}{N}. \tag{23}$$

Here, the numerator is the root-mean-square vertical velocity; the denominator is the bulk buoyancy frequency defined in (21). L_b is an approximation to the distance a representative fluid parcel could be displaced against gravity if all of the kinetic energy contained in its vertical motion were converted to potential energy. Over most of the range of values, L_b and L_T are closely proportional [Fig. 10(b)]. However, the ratio L_b/L_T tends to be significantly smaller than the value of unity estimated from observational data.[69] The decrease of L_b as turbulence decays is limited by the effects of wave motions.

C. Length scales governed by dissipation, buoyancy, and shear

A quantity of central importance in our understanding of turbulence is the kinetic energy dissipation rate,

$$\overline{\epsilon}=2\nu\overline{s_{ij}s_{ij}}, \tag{24}$$

in which

$$s_{ij}=\frac{1}{2}\left(\frac{\partial u'_i}{\partial x_j}+\frac{\partial u'_j}{\partial x_i}\right) \tag{25}$$

is the strain tensor. In the foregoing, primes indicate fluctuations about the horizontal average, and the overbar denotes the volume average over V_s.

Background stratification and shear share the property that their effects on turbulent eddies are felt mainly at large scales. On sufficiently small scales, motions are expected to be independent of these influences,[63] and the definition of ''sufficiently small'' depends on $\overline{\epsilon}$. An estimate of the small-

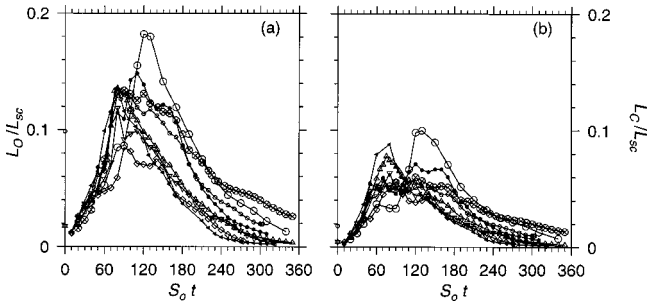

FIG. 11. (a) Ozmidov scale $L_O=\sqrt{\epsilon/N^3}$. (b) Corrsin scale $L_C=\sqrt{\epsilon/S^3}$. $N(t)$ and $S(t)$ are the bulk stratification and shear as described in the text; ϵ is the kinetic energy dissipation rate averaged over V_s. Symbols are as defined in Table I.

est length scale at which eddies are deformed by buoyancy is provided by $r_O L_O$, where r_O is a constant of order unity and L_O is the Ozmidov scale, $L_O=\sqrt{\epsilon/N^3}$.

Numerous investigators[73,74] have suggested that the smallest scale at which eddies are strongly deformed by the mean shear may be estimated as $r_C L_C$, where r_C is a constant of order unity and $L_C=\sqrt{\epsilon/S^3}$. This length is entirely analogous to the above-described Ozmidov scale, and is referred to here as the Corrsin scale. The appropriate numerical values for the constants r_C and r_O are not obvious. Corrsin[73] assigned a value to r_C by assuming that L_C lay within an inertial subrange. In large-scale wind tunnel experiments, Saddoughi and Veeravalli[74] were able to detect anisotropy on scales as small as $0.1L_C$.

These length scales are normally only employed in the context of order-of-magnitude arguments, in which case precise values are unimportant. Here, however, we will find it useful to compare relative magnitudes, so we will need to assign a value to the ratio r_C/r_O. We do so based on the following considerations. If $r_C L_C < r_O L_O$, there exists a range of scales in which deformation by the mean shear is felt, but deformation by buoyancy is not. That condition is equivalent to

$$\mathrm{Ri} < (r_C/r_O)^{-4/3}. \tag{26}$$

This is suggestive of a Richardson number criterion for shear-driven fluctuation growth in the presence of stable stratification. Miles[36] showed that the critical Ri for normal mode instability is 1/4. Simulations of turbulence in uniform shear and stratification[26] have revealed that turbulence is maintained when Ri is less than about 1/4 (depending on the Reynolds number). In the present simulations (as well as in laboratory experiments[31,32]), turbulence decays as Ri increases beyond 1/4, and is extinguished for $\mathrm{Ri}\approx 1/3$. Adopting the latter value for the critical Richardson number, we obtain $r_C/r_O = 3^{3/4} \approx 2.3$. Thus, when the small-scale limits of shear and stratification influences are the same, we expect that L_C will be smaller than L_O by approximately a factor of 2.

Like the overturning scales, L_O and L_C increase rapidly in the early stages of the simulations, then decay (Fig. 11). However, the maximum values of L_O and L_C are attained between $S_0 t = 70$ and 130, significantly later than the time of maximum L_T. This corresponds to the sequence of events described in Sec. III A: The state of maximum overturn size is followed by a breaking event during which turbulence is generated. When turbulence (as quantified by ϵ) is a maximum, so is the size of the spectral region in which eddies are unaffected by the background stratification and shear. As the turbulence decays, these background influences extend to progressively smaller scales.

L_O generally exceeds L_C by about a factor of 2, suggesting that the spectral extents of shear and stratification influences are similar. An exception to this occurs in the earliest phase of the simulation, where L_C/L_O is very small. In this phase, KH instability is growing in the spectral range where strong Reynolds stresses due to shear deformation of eddies draw energy from the background shear rapidly enough to overwhelm the damping influence of buoyancy. The foregoing observations suggest an interesting alternative interpretation of the Richardson number criterion for turbulence generation: $\mathrm{Ri} < \mathrm{Ri}_{cr}$ *is a necessary condition for the existence of a spectral range in which motions are affected by background shear but not by stratification.*

Except at late times when turbulence has decayed, L_O and L_C both tend to be considerably smaller than the overturning scale L_T (cf. Fig. 8). This shows that the largest eddies feel buoyancy and shear effects from the outset, i.e., the onset of buoyancy control occurs at $t=0$. The second major transition in flow physics, the BIV transition, is expected to occur when the effects of background stratification and shear first reach the dissipation subrange, the large-scale limit of which is found near $10L_K$, where $L_K=(\nu^3/\overline{\epsilon})^{1/4}$ is the Kolmogorov scale. This transition will be discussed in sections III D and IV.

D. Summary of length scale evolution

We look now at evolving length scale relationships in two representative simulations. These relationships are illustrated in Fig. 12, which is patterned after the diagrams used to diagnose flow transitions in grid-generated turbulence.[8] Figure 12(a) shows a strongly turbulent case. Throughout the simulation, the Thorpe scale is larger than the Ozmidov scale, indicating that the large eddies are being damped by buoyancy. During the regime of strong turbulence, L_O exceeds $10L_K$ by up to a factor of 5. This indicates a small, but significant range of scales in which inertial accelerations dominate over both buoyancy and viscosity. The BIV transition, at which point $L_O = 10L_K$, occurs later in the simulation, near $S_0 t = 230$. The equivalent scale above which eddies are deformed by the background shear, which we have argued is about twice L_C, enters the dissipation range at about the same time. Another interesting feature appears near $S_0 t = 230$: A large increase in L_T indicates the presence of a secondary overturn in the well-mixed region. While this overturn has significant amplitude, it carries very little potential energy and thus has little effect on subsequent mixing (see the further discussion in Sec IV). Shortly after this point, L_T decreases until it enters the dissipation subrange. Near this point, decay of the three-dimensional displacement

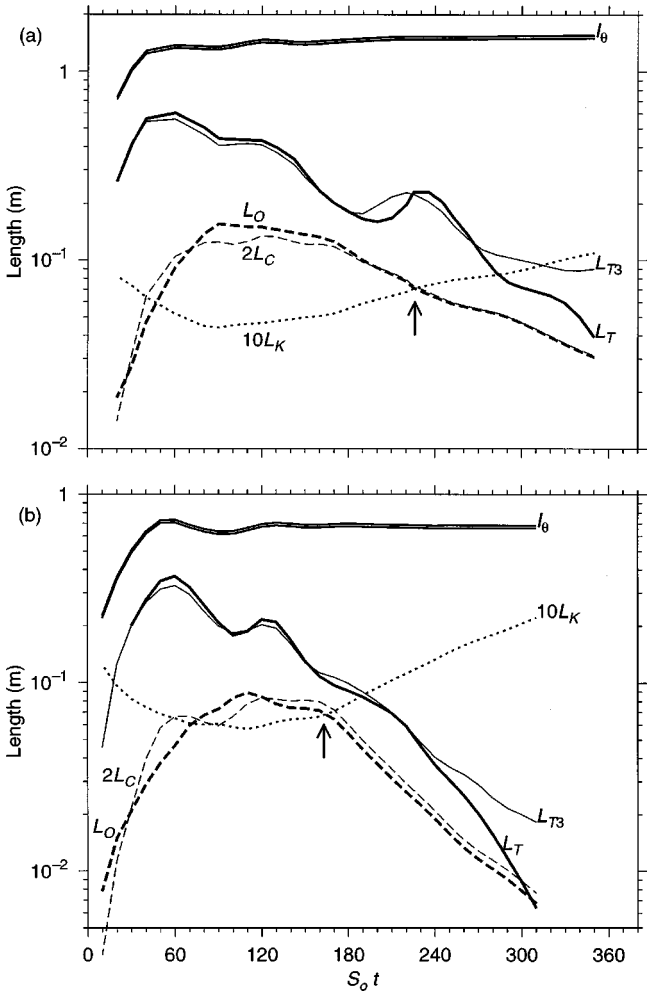

FIG. 12. Length scale diagrams from selected simulations, for comparison with Fig. 1 and with results from grid turbulence experiments (Ref. 8). L_T (thick solid curve) is the Thorpe scale and L_{T3} (thin solid curve) is the three-dimensional displacement scale. L_O (thick dashed curve) and L_C (thin dashed curve) are the Ozmidov and Corrsin scales, respectively. $10L_K$ (dotted line) is the approximate boundary of the dissipation subrange, where L_K is the Kolmogorov scale. Overall layer thickness is indicated by the integral scale l_θ (double curve). Simulations are R16P1 (a) and R04P7 (b). Arrows indicate the BIV transition.

scale L_{T3} slows considerably in comparison to that of L_T. This indicates that the displacement field is now dominated by wave motions rather than overturns.

A high Prandtl number case is shown in Fig. 12(b). In this simulation, the specification Pr=7 necessitated a reduction in the initial Reynolds number, and we note a corresponding reduction in peak turbulence intensity. The intrusion of buoyancy effects into the dissipation range (as indicated by $L_O < 10L_K$) occurs earlier in the simulation than in the previous case. Once again, it is evident from the dominance of L_{T3} over L_T in the late stages that wave motions persist after overturns have vanished.

The results shown in Fig. 12 demonstrate the essential difference between turbulence in a stratified shear layer and turbulence in uniformly stratified and sheared environments. Early in the evolution, results are similar to the shear-dominated case [Fig. 1(b)], i.e., L_O and L_C increase while L_K decreases, so that the spectral range of active turbulence increases. As Ri increases beyond its critical value, however, the behavior begins to resemble the stratification dominated case [Fig. 1(a)]. In this regime, L_O and L_C decrease while L_K increases until turbulence is finally damped at all scales. The tendency of the bulk Richardson number to increase in time thus proves to be the essential element distinguishing turbulence evolution in a stratified shear layer from that occurring in the presence of uniform background gradients.

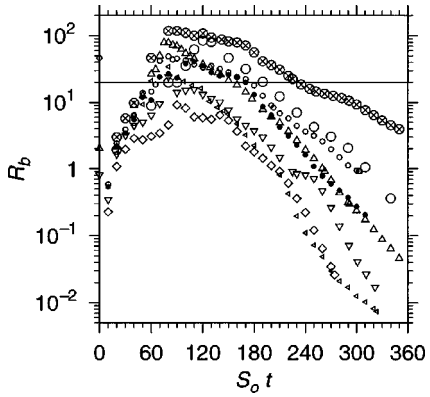

FIG. 13. Evolution of the buoyancy Reynolds number, $R_b = \epsilon/\nu N^2$. Symbols are as defined in Table I. The horizontal line indicates $R_b = 20$, at which buoyancy effects become important in the dissipation range.

IV. CHARACTERIZATIONS OF THE STATE OF THE TURBULENCE

In this section, we describe the flow structure resulting from breaking KH billows in terms of five independent dimensionless quantities, the buoyancy Reynolds number, the shear Reynolds number, the microscale Reynolds number, the Cox number, and the length scale ratio, $R_{OT} = L_O/L_T$. We will then explore relationships among these quantities, and use these relationships to characterize the different phases of turbulence evolution.

The ratio of the Ozmidov scale to the Kolmogorov scale indicates the range of length scales over which motions are free of both the buoyancy force that damps the larger scales and the viscous dissipation that affects the small scales. The buoyancy Reynolds number is the four-thirds power of that ratio:

$$R_b = \left(\frac{L_O}{L_K}\right)^{4/3} = \frac{\overline{\epsilon}}{\nu N^2}. \tag{27}$$

This quantity has been used extensively in studies of stratified turbulence. Various investigators have proposed that active turbulence is present only when R_b exceeds a certain critical value, which is approximately 20. In the present simulations, R_b achieves a maximum value as the transition to turbulence is completed, then decays. Maximum values for the different runs range between $O(10^1)$ and $O(10^2)$ (Fig. 13). This maximum quantifies the main limitation of DNS technology in the study of stratified turbulence: Buoyancy Reynolds numbers found in geophysically relevant flows range from values similar to those attained here to values several orders of magnitude larger.[69,75] Thus, present day computers are able to reproduce only the low-R_b end of

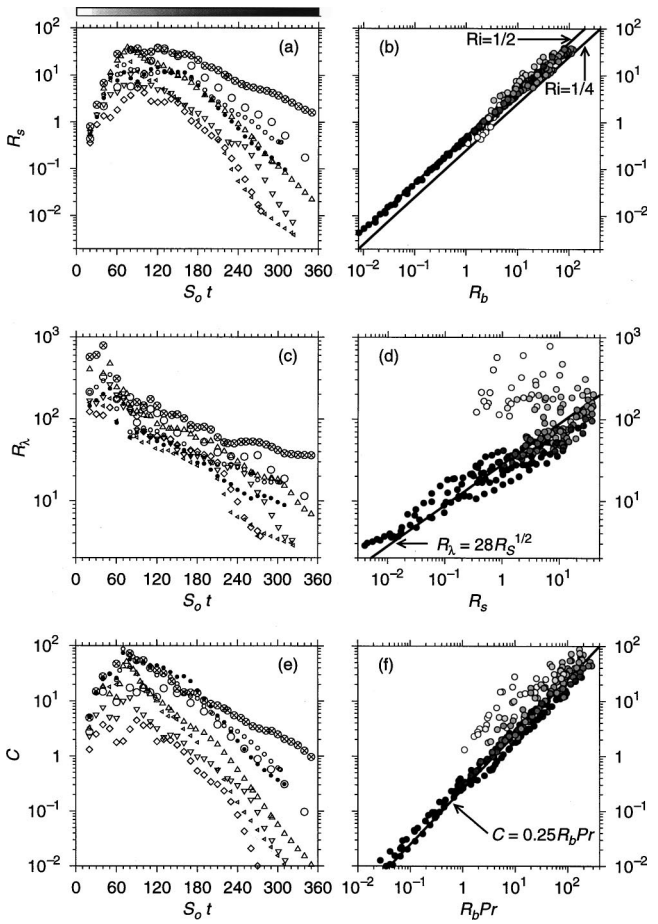

FIG. 14. Alternative measures of the range of active length scales (left column) and relationships among them (right column). In the left column [(a), (c), and (e)], the ordinate is time, and symbols denote different simulations as in previous figures (see Table I). In the right column [(b), (d), and (f)], different ordinates are employed, and time evolution is instead indicated by the shading of the symbols [cf. grayscale above (a)]. The top row shows the shear Reynolds number vs time (a) and vs buoyancy Reynolds number (b). The middle row shows the microscale Reynolds number vs time (c) and vs shear Reynolds number (d). The bottom row shows the Cox number vs time (e) and R_bPr (f).-

the range of turbulent flows found in nature. The weakest simulations, R03P1 and R04P1, never attain the critical value $R_b=20$. Buoyancy Reynolds numbers in all eight simulations eventually drop below the critical value as turbulence is extinguished. (This corresponds to the BIV transition discussed in Sec. III.)

In analogy with R_b, we define a shear Reynolds number, R_s, such that $R_s=(L_C/L_K)^{4/3}$, i.e.,

$$R_s=\frac{\overline{\epsilon}}{\nu S^2}. \tag{28}$$

This quantity has proved highly useful for the characterization of turbulence in sheared environments[73,74] because it indicates the range of length scales that are free of both viscous damping and distortion by the mean shear. In the present simulations, the evolution of R_s closely parallels that of R_b [Figs. 14(a) and 14(b)]. This close relationship is not surprising, since the ratio R_s/R_b is just the bulk Richardson number, whose value remains within a relatively small range.

The microscale Reynolds number is defined using the squared turbulent velocity $q^2=\overline{u'^2}+\overline{v'^2}+\overline{w'^2}$ and the Taylor microscale, $\lambda=\sqrt{5\nu q^2/\epsilon}$, viz.

$$R_\lambda=\frac{q\lambda}{\nu}. \tag{29}$$

In the present simulations, R_λ attains maximum values between $O(10^2)$ and $O(10^3)$ early in the flow evolution, before the transition to turbulence [Fig. 14(c)]. This is because the perturbation kinetic energy $\frac{1}{2}q^2$ represents only weakly dissipative, nonstationary wave motions during this regime. After transition, R_λ decreases from $O(10^2)$, a value comparable to those attained in contemporary DNS of stationary, isotropic turbulence.[58]

In a state of production-dissipation balance, it may be shown[73] that R_λ is related to the shear Reynolds number by

$$R_\lambda=\frac{\sqrt{5R_s}}{b_{13}(1-R_f)}, \tag{30}$$

in which b_{13} is minus the ratio of the turbulent momentum flux $\overline{u'w'}$ to q^2 and R_f is the flux Richardson number. With the common approximations $b_{13}=0.10$ and $R_f=0.2$, we obtain $R_\lambda\approx 28\sqrt{R_s}$. Early in the KH life cycle, R_λ exceeds this estimate by more than an order of magnitude [Fig. 14(d)], due mainly to the fact that the disturbance is dominated by wave motions and is far from a state of production-dissipation balance. During the decay phase, however, R_λ remains close to $28\sqrt{R_s}$.

A fourth nondimensional quantity that is used commonly to characterize stratified turbulence is the Cox number, defined here by

$$C=\frac{\overline{|\nabla\theta'|^2}}{\theta_{0z}^2}. \tag{31}$$

Whereas R_s is proportional to the ratio of kinetic energy dissipation by the disturbance to that accomplished by the mean flow, C is the ratio of the rate of scalar variance dissipation, χ, generated by the disturbance to that generated by the mean flow. The Cox number attains a maximum just as the transition to turbulence is completed, i.e., slightly earlier than the maxima of R_b and R_s, then decays [Fig. 14(e)]. In stationary, homogeneous, stably stratified turbulence, it may be shown that

$$\frac{C}{R_b\mathrm{Pr}}=\frac{\kappa CN^2}{\overline{\epsilon}}=\frac{R_f}{1-R_f} \tag{32}$$

in which R_f is the flux Richardson number.[23] The standard estimate $R_f=0.2$[18] results in $C=0.25\,R_b\,\mathrm{Pr}$. This relation is shown by the straight line in Fig. 14(f). Except during the early, preturbulent phase, this approximation describes our results accurately.

A quantity that has often been suggested as a convenient indicator of the age of a geophysical turbulent event is the length scale ratio $R_{OT}=L_O/L_T$.[16,23,25,70] Gibson[16] suggests

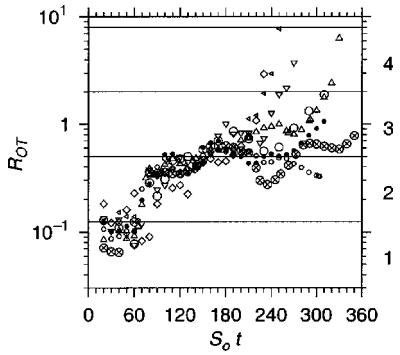

FIG. 15. The length scale ratio $R_{OT}=L_O/L_T$, vs time. Horizontal lines indicate the classification scheme employed by WD (Ref. 25).

that, for turbulent events in the ocean, R_{OT} decreases in time from values $\gg 1$ to values $\ll 1$. While this scenario has been observed in laboratory experiments on grid-generated turbulence, its validity for the case of shear instability is questionable. Wijesekera and Dillon (WD)[25] have proposed an alternative scenario in which the time evolution of R_{OT} proceeds in the opposite sense, i.e., from small to large. This lack of consensus on the evolution of R_{OT} is a major obstacle to the interpretation of geophysical turbulence measurements.[6]

WD organized a large number of observations of turbulent patches from the ocean thermocline into five classes, from small to large R_{OT}, and showed that the Shannon entropy is larger for the events with larger R_{OT}. Combined with the expectation that entropy increases with time, this result suggests that the latter possibility described above, i.e., that R_{OT} should increase with time, is the correct one. Here, we find a similar result in a more explicit form; the general pattern in all simulations is for R_{OT} to increase with time [Fig. 15(a)]. In all of our simulations, the tendency is for flows to fall into WD's class 1 ($R_{OT}<0.125$) during the initial rollup and pairing phases. The transition to turbulence is accompanied by a rapid increase in R_{OT} to values in the upper range of WD's class 2 (near $S_0t=60-90$). From $S_0t \approx 90$ to $S_0t \approx 210$, R_{OT} increases slowly into the lower range of WD's class 3 ($0.5<R_{OT}<2$). Beyond this point, the scatter between different simulations increases considerably, but the overall tendency is for R_{OT} to continue to increase through class 3 and often into class 4 ($2<R_{OT}<8$). Part of this scatter may be due to the fact that both L_O and L_T become very small during the late phases of the simulations, so that their ratio is difficult to compute accurately. Also, values of L_T comparable to the grid spacing are susceptible to contamination by numerical noise. Interestingly, the evolution of R_{OT} illustrated in Fig. 15(a) appears to be independent of the Prandtl number.

An interesting anomaly occurred in simulation R15P1 [circled crosses on Fig. 15(a)]: near $S_0t=190$, the evolution of R_{OT} exhibited a dramatic reversal which lasted until approximately $S_0t=240$. This reversal corresponded to the occurrence of a new KH instability within the well-mixed region at the center of the vertical domain. This secondary overturning event was made possible by the tendency for density to mix more thoroughly than velocity in the center of the turbulent layer, so that the gradient Richardson number is locally small.[45] Although its Thorpe displacement is significant, it contains very little potential energy, since its surroundings are nearly homogeneous.

V. CONCLUSIONS

For a wide range of initial conditions, the bulk Richardson number Ri evolves toward an approximately universal value which is slightly in excess of 1/4. (This value depends somewhat on the convention used to define Ri. If maximum gradients of velocity and density are used, the final value is near 0.32, as has been found previously in laboratory experiments.[31,32] If average gradients are used, the value is closer to 0.45.) This behavior suggests a length scale, $L_{sc}=u_0^2/4g\theta_0$, which encompasses much of the dependence of the evolutionary patterns of the various length scales on the initial conditions.

Both the one-dimensional Thorpe scale, L_T, and its three-dimensional counterpart, L_{T3}, increase to maxima as the transition to turbulence begins, then decrease to near zero as the turbulence decays. When the flow is dominated by turbulent overturns, L_T and L_{T3} are nearly equal. Once the overturns have subsided, however, values of L_{T3} exceeding those of L_T reflect the continued presence of stable wave motions.

The interaction of shear and stratification in a vertically localized layer is fundamentally different from that found in the case of uniform background gradients. The source of the difference is that the bulk Richardson number is constant in the case of uniform gradients, but increases in time in the case of the localized layer. In each case, a critical value of the bulk Richardson number, $\mathrm{Ri}_{cr}\approx 1/4$, divides the parameter space into two distinct regimes. In each case, $\mathrm{Ri}>\mathrm{Ri}_{cr}$ leads to the decay of any turbulence initially present. When $\mathrm{Ri}<\mathrm{Ri}_{cr}$ in the uniform gradient case, turbulence evolves much as in the unstratified case: The infinite supply of kinetic energy in the background shear allows buoyancy effects to be confined to the largest scales, and turbulence grows without limit. When $\mathrm{Ri}<\mathrm{Ri}_{cr}$ in the localized case, turbulence grows initially as in the unstratified case. Ri increases in time, though, and eventually exceeds Ri_{cr}. Beyond this point, the stratification (however small initially) overwhelms the shear and causes the turbulence to decay much as in the case of pure stratification.

The onset of buoyancy control is not a useful concept for understanding shear layer evolution, since the largest scales of motion are controlled by buoyancy from the outset. The BIV transition, however, does occur as R_b drops below a critical value near 25 and large-scale influences are felt in the dissipation range. In terms of length scale evolution, we have seen no qualitative change in turbulence structure as the BIV transition is crossed.

We have seen that, in the present model of turbulence resulting from shear instability, the length scale ratio $R_{OT}=L_O/L_T$ is small when the flow is dominated by large, nondissipative overturns and large in regimes where overturning has been damped. The former states tend to occur early in the flow evolution (i.e., they correspond to WD's ''natal'' turbu-

lence). R_{OT} may also be small during secondary overturning events. The latter occur late in our simulations, but are physically similar to the overturns that occur near $t=0$. In summary, these results suggest, within the limitations of the present mathematical model of geophysical turbulence, that ''young'' turbulent events may be identified by values of R_{OT} less than unity, mature events by values greater than unity.

ACKNOWLEDGMENTS

This research was funded by the National Science Foundation under Grant No. OCE9521359. Computations were performed on the Connection Machine CM5 facility at Oregon State University's Environmental Computing Center.

[1]S. Thorpe, ''Transition phenomena and the development of turbulence in stratified fluids,'' J. Geophys. Res. **92**, 5231 (1987).
[2]M. C. Gregg, ''Diapycnal mixing in the thermocline: A review,'' J. Geophys. Res. **92**, 5249 (1987).
[3]H. Fernando, ''Turbulent mixing in stratified fluids,'' Annu. Rev. Fluid Mech. **23**, 455 (1991).
[4]D. Caldwell and J. Moum, ''Turbulence and mixing in the ocean,'' Rev. Geophys. **33**, 1385 (1995).
[5]H. Seim and M. Gregg, ''Detailed observations of a naturally-occurring shear instability,'' J. Geophys. Res. **99**(C5), 10,049 (1994).
[6]I. DeSilva, H. Fernando, F. Eaton, and D. Hebert, ''Evolution of Kelvin–Helmholtz billows in nature and laboratory,'' Earth Planet. Sci. Lett. **143**, 217 (1996).
[7]C. Sun, W. Smyth, and J. Moum, ''Dynamic instability of stratified shear flow in the upper equatorial Pacific,'' J. Geophys. Res. **103**, 10323 (1998).
[8]D. Stillinger, K. Helland, and C. Van Atta, ''Experiments on the transition of homogeneous turbulence to internal waves in a stratified fluid,'' J. Fluid Mech. **131**, 91 (1983).
[9]E. Itsweire, K. Helland, and C. Van Atta, ''The evolution of grid-generated turbulence in a stably-stratified fluid,'' J. Fluid Mech. **162**, 299 (1986).
[10]J. Rohr, E. Itsweire, K. Helland, and C. Van Atta, ''Growth and decay of turbulence in a stably stratified shear flow,'' J. Fluid Mech. **195**, 77 (1988).
[11]J. Lienhard and C. Van Atta, ''The decay of turbulence in thermally-stratified flow,'' J. Fluid Mech. **210**, 57 (1990).
[12]P. Picirillo and C. Van Atta, ''The evolution of a uniformly sheared thermally stratified turbulent flow,'' J. Fluid Mech. **334**, 61 (1997).
[13]F. Jacobitz, S. Sarkar, and C. Van Atta, ''Direct numerical simulations of the turbulence evolution in a uniformly sheared and stratified flow,'' J. Fluid Mech. **342**, 231 (1997).
[14]C. Gibson, ''Fossil temperature, salinity and vorticity turbulence in the ocean,'' in *Marine Turbulence*, edited by J. Nihoul (Elsevier, New York, 1980), pp. 221–257.
[15]C. Gibson, ''Alternative interpretations for microstructure patches in the thermocline,'' J. Phys. Oceanogr. **12**, 374 (1982).
[16]C. Gibson, ''Fossil turbulence and intermittency in sampling oceanic mixing processes,'' J. Geophys. Res. **92**, 5383 (1987).
[17]C. Gibson, ''Laboratory, numerical and oceanic fossil turbulence in rotating and stratified flows,'' J. Geophys. Res. **96**, 12,549 (1991).
[18]G. Ivey and J. Imberger, ''On the nature of turbulence in a stratified fluid. I. The energetics of mixing,'' J. Phys. Oceanogr. **21**, 650 (1991).
[19]J. Imberger and G. Ivey, ''On the nature of turbulence in a stratified fluid. II. Application to lakes,'' J. Phys. Oceanogr. **21**, 659 (1991).
[20]S. Tavoularis, ''Asymptotic laws for transversely homogeneous turbulent shear flows,'' Phys. Fluids **28**, 999 (1985).
[21]W. Smyth, P. Zavialov, and J. Moum, ''Decay of turbulence in the upper ocean following sudden isolation from surface forcing,'' J. Phys. Oceanogr. **27**, 810 (1997).
[22]D. Caldwell, ''Oceanic turbulence: Big bangs or continuous creation?'' J. Geophys. Res. **88**, 7543 (1983).
[23]T. Dillon, ''The energetics of overturning structures: Implications for the theory of fossil turbulence,'' J. Phys. Oceanogr. **14**, 541 (1984).
[24]C. Gibson, ''Oceanic turbulence: Big bangs and continuous creation,'' J. Physicochem. Hydrodyn. **8**, 1 (1987).
[25]H. Wijesekera and T. Dillon, ''Shannon entropy as an indicator of age for turbulent overturns in the oceanic thermocline,'' J. Geophys. Res. **102**, 3279 (1997).
[26]S. Holt, J. R. Koseff, and J. Ferziger, ''A numerical study of the evolution and structure of homogeneous stably stratified sheared turbulence,'' J. Fluid Mech. **237**, 499 (1992).
[27]E. Itsweire, J. Koseff, D. Briggs, and J. Ferziger, ''Turbulence in stratified shear flows: Implications for interpreting shear-induced mixing in the ocean,'' J. Phys. Oceanogr. **23**, 1508 (1993).
[28]G. Brown and A. Roshko, ''On density effects and large structure in turbulent mixing layers,'' J. Fluid Mech. **64**, 775 (1974).
[29]R. Breidenthal, ''Structure in turbulent mixing layers and wakes using a chemical reaction,'' J. Fluid Mech. **109**, 1 (1981).
[30]J. Lasheras and H. Choi, ''Three-dimensional instability of a plane, free shear layer: An experimental study of the formation and evolution of streamwise vortices,'' J. Fluid Mech. **189**, 53 (1988).
[31]S. Thorpe, ''Turbulence in stably stratified fluids: A review of laboratory experiments,'' Boundary-Layer Meteorol. **5**, 95 (1973).
[32]C. Koop and F. Browand, ''Instability and turbulence in a stratified layer with shear,'' J. Fluid Mech. **93**, 135 (1979).
[33]G. Lawrence, F. Browand, and L. Redekopp, ''Stability of a sheared density interface,'' Phys. Fluids A **3**, 2360 (1991).
[34]G. Taylor, ''Effect of variation in density on the stability of superposed streams of fluid,'' Proc. R. Soc. London, Ser. A **132**, 499 (1931).
[35]S. Goldstein, ''On the stability of superposed streams of fluid of different densities,'' Proc. R. Soc. London, Ser. A **132**, 524 (1931).
[36]J. Miles, ''On the stability of heterogeneous shear flows,'' J. Fluid Mech. **10**, 496 (1961).
[37]P. Hazel, ''Numerical studies of the stability of inviscid parallel shear flows,'' J. Fluid Mech. **51**, 39 (1972).
[38]R. Pierrehumbert and S. Widnall, ''The two- and three-dimensional instabilities of a spatially periodic shear layer,'' J. Fluid Mech. **114**, 59 (1982).
[39]G. Klaassen and W. Peltier, ''The onset of turbulence in finite-amplitude Kelvin–Helmholtz billows,'' J. Fluid Mech. **155**, 1 (1985).
[40]H. Abarbanel, D. Holm, J. Marsden, and T. Ratiu, ''Nonlinear stability analysis of stratified fluid equilibria,'' Philos. Trans. R. Soc. London **318**, 349 (1986).
[41]G. Klaassen and W. Peltier, ''The influence of stratification on secondary instability in free shear layers,'' J. Fluid Mech. **227**, 71 (1991).
[42]P. Patnaik, F. Sherman, and G. Corcos, ''A numerical simulation of Kelvin–Helmholtz waves of finite amplitude,'' J. Fluid Mech. **73**, 215 (1976).
[43]R. Metcalfe, S. Orszag, M. Brachet, S. Menon, and J. Riley, ''Secondary instability of a temporally-growing mixing layer,'' J. Fluid Mech. **184**, 207 (1987).
[44]C. Caulfield and W. Peltier, ''Three-dimensionalization of the stratified mixing layer,'' Phys. Fluids **6**, 3803 (1994).
[45]J. Scinocca, ''The mixing of mass and momentum by Kelvin–Helmholtz billows,'' J. Atmos. Sci. **52**, 2509 (1995).
[46]D. Fritts, T. Palmer, O. Andreassen, and I. Lie, ''Evolution and breakdown of Kelvin–Helmholtz billows in stratified compressible flows. 1. Comparison of two- and three-dimensional flows,'' J. Atmos. Sci. **53**, 3173 (1996).
[47]T. Palmer, D. Fritts, and O. Andreassen, ''Evolution and breakdown of Kelvin–Helmholtz billows in stratified compressible flows. 2. Instability structure, evolution and energetics,'' J. Atmos. Sci. **53**, 3192 (1996).
[48]G. Corcos and S. Lin, ''The mixing layer: Deterministic models of a turbulent flow. 2. The origin of the three-dimensional motion,'' J. Fluid Mech. **139**, 67 (1984).
[49]M. Rogers and R. Moser, ''The three-dimensional evolution of a plane mixing layer: The Kelvin–Helmholtz rollup,'' J. Fluid Mech. **243**, 183 (1992).
[50]R. Moser and M. Rogers, ''The three-dimensional evolution of a plane mixing layer: Pairing and transition to turbulence,'' J. Fluid Mech. **247**, 275 (1993).
[51]A. Cortesi, G. Yadigaroglu, and S. Banerjee, ''Numerical investigation of the formation of three-dimensional structures in stably-stratified mixing layers,'' Phys. Fluids **10**, 1449 (1998).
[52]A. Cortesi, B. Smith, G. Yadigaroglu, and S. Banerjee, ''Numerical investigation of the entrainment and mixing processes in neutral and stably-stratified mixing layers,'' Phys. Fluids **11**, 162 (1999).

[53]W. Geyer and J. Smith, ''Shear instability in a highly stratified estuary,'' J. Phys. Oceanogr. **17**, 1668 (1987).
[54]W. Smyth, G. Klaassen, and W. R. Peltier, ''Finite amplitude Holmboe waves,'' Geophys. Astrophys. Fluid Dyn. **43**, 181 (1988).
[55]W. Smyth and W. Peltier, ''Instability and transition in Kelvin–Helmholtz and Holmboe waves,'' J. Fluid Mech. **228**, 387 (1991).
[56]W. Smyth and W. Peltier, ''Two-dimensional turbulence in homogeneous and stratified shear layers,'' Geophys. Astrophys. Fluid Dyn. **69**, 1 (1993).
[57]G. Klaassen and W. Peltier, ''The role of transverse secondary instabilities in the evolution of free shear layers,'' J. Fluid Mech. **202**, 367 (1989).
[58]P. Moin and K. Mahesh, ''Direct numerical simulation: A tool in turbulence research,'' Annu. Rev. Fluid Mech. **30**, 539 (1998).
[59]W. Smyth and W. Peltier, ''The transition between Kelvin–Helmholtz and Holmboe instability: An investigation of the overreflection hypothesis,'' J. Atmos. Sci. **46**, 3698 (1989).
[60]N. Oakey, ''Determination of the rate of dissipation of turbulent energy from simultaneous temperature and velocity shear microstructure measurements,'' J. Phys. Oceanogr. **12**, 256 (1982).
[61]S. Panchev and D. Kesich, ''Energy spectrum of isotropic turbulence at large wave numbers,'' Comptes rendus de l'Acadèmie bulgare des Sciences **22**, 627 (1969).
[62]W. Smyth, ''Dissipation range geometry and scalar spectra in sheared, stratified turbulence,'' J. Fluid Mech. **401**, 209 (1999).
[63]W. Smyth and J. Moum, ''Anisotropy of turbulence in stably stratified mixing layers,'' Phys. Fluids **12**, 1343 (2000).
[64]G. K. Batchelor, ''Small-scale variation of convected quantities like temperature in turbulent fluid,'' J. Fluid Mech. **5**, 113 (1959).
[65]R. Kraichnan, ''Small-scale structure of a scalar field convected by turbulence,'' Phys. Fluids **11**, 945 (1968).
[66]D. Bogucki, J. Domaradzki, and P. Yeung, ''Direct numerical simulations of passive scalars with Pr>1 advected by turbulent flow,'' J. Fluid Mech. **343**, 111 (1997).
[67]J. N. Moum, ''Efficiency of mixing in the main thermocline,'' J. Geophys. Res. **101**, 57 (1996).
[68]S. Thorpe, ''Turbulence and mixing in a Scottish loch,'' Philos. Trans. R. Soc. London **286**, 125 (1977).
[69]J. Moum, ''Energy-containing scales of turbulence in the ocean thermocline,'' J. Geophys. Res. **101**, 14095 (1996).
[70]T. Dillon, ''Vertical overturns: A comparison of Thorpe and Ozmidov scales,'' J. Geophys. Res. **87**, 9601 (1982).
[71]K. Winters, P. Lombard, J. Riley, and E. A. D'Asaro, ''Available potential energy and mixing in density-stratified fluids,'' J. Fluid Mech. **289**, 115 (1995).
[72]E. Itsweire, ''Measurements of vertical overturns in a stably stratified turbulent flow,'' Phys. Fluids **27**, 764 (1984).
[73]S. Corrsin, ''Local isotropy in turbulent shear flow,'' N.A.C.A. RM58B11 (1958).
[74]S. Saddoughi and S. Veeravalli, ''Local isotropy in turbulent boundary layers at high Reynolds number,'' J. Fluid Mech. **268**, 333 (1994).
[75] A. Gargett, T. Osborn, and P. Nasmyth, ''Local isotropy and the decay of turbulence in a stratified fluid,'' J. Fluid Mech. **144**, 231 (1984).
[76]C. Gibson and W. Schwarz, ''The universal equilibrium spectra of turbulent velocity and scalar fields,'' J. Fluid Mech. **16**, 365 (1963).